A Direct Sampling Method for Inverse Electromagnetic Medium Scattering

Kazufumi Ito* Bangti Jin† Jun Zou‡

August 5, 2013

Abstract

In this paper, we study the inverse electromagnetic medium scattering problem of estimating the support and shape of medium scatterers from scattered electric/magnetic near-field data. We shall develop a novel direct sampling method based on an analysis of electromagnetic scattering and the behavior of the fundamental solution. It is applicable to a few incident fields and needs only to compute inner products of the measured scattered field with the fundamental solutions located at sampling points. Hence it is strictly direct, computationally very efficient, and highly robust to the presence of data noise. Two- and three-dimensional numerical experiments indicate that it can provide reliable support estimates for multiple scatterers in case of both exact and highly noisy data.

Key Words: inverse medium scattering, direct sampling method, scattering analysis, electromagnetic wave propagation

1 Introduction

Inverse electromagnetic scattering represents an important noninvasive imaging technology for interrogating material properties, and it arises in many practical applications such as biomedical diagnosis [7], nondestructive testing [34], and geophysical exploration [14]. In this work we are concerned with the inverse medium scattering problem of determining electrical/magnetic properties of unknown inhomogeneous objects embedded in a homogeneous background from noisy measurements of the scattered electric/magnetic field corresponding to one or several incident fields impinged on the objects. Mathematically, the scattering problem is described by the time-harmonic Maxwell system:

$$\begin{aligned} \mathrm{i}\omega\epsilon\, E + \nabla \times H = 0 \quad &\text{in } \mathbb{R}^{\mathrm{d}}, \\ -\mathrm{i}\omega\mu\, H + \nabla \times E = 0 \quad &\text{in } \mathbb{R}^{\mathrm{d}}, \end{aligned}$$

where the vectorial fields H and E denote the magnetic and electric fields, respectively. Here the constant ω is the angular frequency, the functions ϵ and μ refer to the electrical permittivity and magnetic permeability, respectively.

Let the domain $\Omega \subset \mathbb{R}^{\mathrm{d}}$ ($\mathrm{d} = 2, 3$) be the space occupied by the inhomogeneous medium objects within the homogeneous background $\mathbb{R}^{\mathrm{d}}$. We are interested in either electrical or magnetic inhomogeneities, but shall focus our discussions on the case of electrical inhomogeneities since the case of magnetic inhomogeneities follows analogously. So we shall assume $\mu = \mu_0$, with μ_0 being the magnetic permeability of the background. Then by taking the curl of the second equation of the system and eliminating H in the first equation, we obtain the following vector Helmholtz equation for the electric field E

$$\nabla \times (\nabla \times E) - k^2 n^2(x)\, E = 0, \tag{1}$$

*Department of Mathematics and Center for Research in Scientific Computation, North Carolina State University, Raleigh, North Carolina (kito@unity.ncsu.edu).

†Department of Mathematics, Texas A&M University, College Station, Texas 77843-3368, USA (bangti.jin@gmail.com).

‡Department of Mathematics, The Chinese University of Hong Kong, Shatin, N.T., Hong Kong (zou@math.cuhk.edu.hk).

where k is the wavenumber, with $k^2 = \omega^2\epsilon_0\mu_0$ (ϵ_0 is the background electrical permittivity), and $n = \frac{1/\sqrt{\epsilon_0\mu_0}}{1/\sqrt{\epsilon\mu_0}}$ is the refractive index function, i.e., the ratio of the wave velocity in the homogeneous background to that in the medium with inhomogeneities. The refractive index n completely characterizes the inhomogeneities, with a support $\mathrm{supp}(n^2-1) = \Omega$. Further, we assume that the medium scattering problem is excited by an incident plane wave E^i:

$$E^i = pe^{\mathrm{i}kd\cdot x},$$

where $d \in \mathbb{S}^{\mathrm{d}-1}$ and $p \in \mathbb{S}^{\mathrm{d}-1}$ are the incident direction and polarization, respectively. Since the incident field E^i is solenoidal, i.e., $\nabla \cdot E^i = 0$, the polarization p should be chosen such that it is perpendicular to the incident direction d. Then the incident field E^i satisfies the Maxwell system (1) in the entire homogeneous space $\mathbb{R}^{\mathrm{d}}$. The forward scattering problem is to find the total electric field E given the refractive index n^2 and the following Silver-Müller radiation condition for the scattered field $E^s = E - E^i$:

$$\lim_{|x|\to\infty} |x|^{\frac{\mathrm{d}-1}{2}} \left(\nabla \times E^s \times \widehat{x} - \mathrm{i}kE^s\right) = 0$$

uniformly for all directions $\widehat{x} = x/|x| \in \mathbb{S}^{\mathrm{d}-1}$.

The inverse problem of our interest is the inverse medium scattering problem, which is to reconstruct the inhomogeneous media from the scattered electric field E^s corresponding to one (or several) incident field E^i, measured over a certain closed curve/surface Γ. Due to the practical significance of the inverse problem, there has been considerable interest in designing efficient and stable inversion techniques. However, this is very challenging because of a number of complicating factors: strong nonlinearity of the map from the refractive index to the scattered field, severe ill-posedness of the inverse problem, complexity of the forward model, and the limited availability of (noisy) data. Nonetheless, a large number of inverse scattering methods have been developed in the literature, which can be roughly divided into two categories: direct and indirect methods. The former aims at detecting the scatterer support and shape, and includes linear sampling method (LSM) [12, 8], multiple signal classification (MUSIC) [16, 5, 3, 9], and factorization method [24] [25, Chapter 5]. In contrast, the latter provides a distributed estimate of the refractive index n^2 by applying regularization techniques. We just mention adjoint-based method [17, 33, 26], recursive linearization (for multi-frequency data) [6], Gauss-Newton method [20, 15, 21], contrasted source inversion [2], and level set method [18] for an incomplete list. Generally, the estimates by a method from the latter group can provide more details of inclusions/inhomogeneities, but at the expense of much increased computational efforts, especially when the forward model is the full three-dimensional Maxwell system.

In this work, we develop a direct sampling method (DSM) for stably and accurately detecting the scatterer support. It was first developed for the inverse acoustic scattering problems with near-field data [22]; see also the closely related orthogonality sampling [30] for the far-field data. In [28], the performance of the DSM using near-field and far-field data was evaluated and its effectiveness was also studied for other scattering scenarios, e.g., obstacles, inhomogeneous media and cracks. The goal of this work is to extend the DSM to electromagnetic scattering. Due to the much increased complexity of the Maxwell system relative to its scalar counterpart, the Helmholtz equation, the extension is nontrivial and requires several innovations. It is based on an integral representation of the scattered field, a careful analysis on electromagnetic scattering and the behavior of the fundamental solution. Numerically, it involves only computing inner products of the measured scattered field E^s with fundamental solutions to the Maxwell system located at sampling points over the measurement surface Γ. Hence it is strictly direct and does not involve any matrix operations, and its implementation is straightforward and embarrassingly parallel. Our extensive numerical experiments indicate that it can provide an accurate and reliable estimate of the scatterer support, even in the presence of a fairly large amount of random noise in the data. Hence, it represents an effective yet simple computational tool for reliable support detection. In practice, a rough estimate of the scatterer support may be sufficient for many purposes [32]. If desired, one can obtain an enhanced estimate by other indirect scattering methods [23], using the DSM estimate to determine a small computational domain. Since indirect methods often involve expensive nonlinear optimization processes, a small initial domain can essentially reduce the overall computational efforts.

The rest of the paper is organized as follows. In Section 2, we recall an integral reformulation of the Maxwell system recently derived in [27], which plays an essential role in the derivation of the DSM. Then we develop the method in Section 3 in detail, where a preliminary analysis of its theoretical performance is also provided. In Section 4, we provide two- and three-dimensional numerical experiments to illustrate its accuracy and robustness for both exact and noisy data. Technical details of the forward scattering simulation are provided in the appendix.

2 Integral representation of Maxwell System

In this part, we recall an equivalent integral formulation of the Maxwell system (1), which is fundamental to the derivation of the direct sampling method. We begin with the definition of the fundamental solution $G(x, y)$ to the scalar Helmholtz equation, i.e.,

$$(-\Delta - k^2)G(x, y) = \delta(x - y),$$

where $\delta(x - y)$ is the Dirac delta function with the singularity located at $y \in \mathbb{R}^{\mathrm{d}}$. We know that $G(x, y)$ has the following representation (see, e.g., [13])

$$G(x, y) = \begin{cases} \dfrac{\mathrm{i}}{4} H_0^{(1)}(k|x - y|), & \mathrm{d} = 2, \\ \dfrac{1}{4\pi} \dfrac{e^{\mathrm{i}k|x-y|}}{|x - y|}, & \mathrm{d} = 3, \end{cases}$$

where the function $H_l^{(1)}$ refers to Hankel's function of the first kind and lth order. Using the scalar function $G(x, y)$ we can define a matrix-valued function $\Phi(x, y)$ by

$$\Phi(x, y) = k^2 G(x, y)\, I + D^2 G(x, y), \tag{2}$$

where $I \in \mathbb{R}^{\mathrm{d}\times\mathrm{d}}$ is the identity matrix and $D^2 G$ denotes the Hessian of G. Then we can verify by some direct calculations that $\nabla \cdot \Phi(x, y) = 0$ and

$$\nabla \times \nabla \times \Phi(x, y) - k^2 \Phi(x, y) = \delta(x - y) I, \tag{3}$$

where (and in the sequel) the actions of the operators $\nabla\cdot$ and $\nabla\times$ on a matrix-valued function are always understood to be columnwise operation. Hence, the matrix $\Phi(x, y)$ defined by (2) is a divergence-free fundamental solution to the Maxwell system (1) in the homogeneous space $\mathbb{R}^{\mathrm{d}}$. Using the fundamental solution $\Phi(x, y)$, the total electric field $E(x)$ can be represented by the following integral equation

$$E(x) = E^i + \int_{\mathbb{R}^{\mathrm{d}}} \Phi(x, y)(n^2 - 1)E(y)dy. \tag{4}$$

We note that the fundamental solution $\Phi(x, y)$ involves a non-integrable singularity at $x = y$. Hence care must be exerted when interpreting the integral when the point x lies within the domain Ω [19]. Next we let $\eta = n^2 - 1$, which precisely characterizes the inhomogeneities in the medium. In particular, the support of η coincides with the scatterer support Ω. Furthermore, we introduce the function $J = (n^2 - 1)E$, i.e., the induced electrical current caused by the medium inhomogeneities. Then, the total electric field $E(x)$ satisfies [13, Theorem 9.1]

$$E(x) = E^i(x) + k^2 \int_{\mathbb{R}^{\mathrm{d}}} G(x, y)J(y)\, dy + \nabla_x \int_{\mathbb{R}^{\mathrm{d}}} G(x, y)\mathrm{div}_y J(y)\, dy.$$

Upon noting the reciprocity relation $\nabla_x G(x, y) = -\nabla_y G(x, y)$ and applying integration by parts to the last term on the right hand side, we arrive at the following equivalent integral equation

$$E(x) - \int_{\mathbb{R}^{\mathrm{d}}} G(x, y)PJ(y)\, dy = E^i(x),$$

where the operator P is defined by

$$P\phi = k^2 I\phi + \mathrm{grad}(\mathrm{div}\phi).$$

Thus, by multiplying the equation with the coefficient η, we obtain an integral equation for the induced electric current J

$$J(x) - \eta \int_\Omega G(x,y) P J(y)\, dy = \eta E^i(x), \quad x \in \Omega. \tag{5}$$

Equation (5) was rigorously justified in suitable function spaces in [27], and it is very convenient for solving related inverse problems; see [27] for an application to the inverse source problem and [26] for inverse medium scattering. Compared with the whole-space Maxwell system, equation (5) is defined only over the scatterer support Ω since the induced electrical current J vanishes identically outside Ω. This reduces greatly the simulation domain, and hence brings significant computational benefits. We shall adopt (5) for forward scattering simulation, which can be discretized numerically by a mid-point quadrature rule (cf. Appendix A for details).

3 Direct sampling method

In this section, we develop the DSM to determine the locations, number and shape of the scatterers/inhomogeneities in electromagnetic wave propagation. It is based on an analysis of electromagnetic scattering, and extends our earlier work on acoustic scattering [22]. We shall also provide an analysis of its theoretical performance by examining the behavior of the fundamental solution. For the sake of convenience, we introduce the domain Ω_Γ, which is the open domain enclosed by the measurement surface Γ, and use $(\cdot,\cdot)$ for the real inner product on $\mathbb{C}^{\mathrm{d}}$ and the overbar for the complex conjugate.

3.1 Derivation

The derivation relies essentially on the two basic facts. The first is a representation of the scattered electric field E^s using the fundamental solution Φ by, cf. (4):

$$E^s(x) = \int_\Omega \Phi(x,y) J(y) dy \quad \forall\, x \in \Gamma. \tag{6}$$

The second fact is an important relation for the fundamental solution $\Phi(x,y)$ to the Maxwell system (1). For any two arbitrary sampling points x_p and x_q that lie inside the domain Ω_Γ and are far away from the measurement boundary Γ, we have the following approximation

$$\int_\Gamma (\Phi(x,x_p)p, \overline{\Phi}(x,x_q)q) ds \approx k^{-1}(p, \Im(\Phi(x_p,x_q))q) \quad \forall\, p \in \mathbb{C}^{\mathrm{d}},\, q \in \mathbb{R}^{\mathrm{d}}, \tag{7}$$

where $\Im$ denotes taking the imaginary part. Next, we derive this crucial relation. To do so, we first show the following lemma.

Lemma 3.1. *Let x_p and x_q be two distinct points in the domain Ω_Γ, and ν be the unit outward normal direction to the boundary Γ. Then for any constant vectors $p \in \mathbb{C}^{\mathrm{d}}$ and $q \in \mathbb{R}^{\mathrm{d}}$, there holds*

$$\int_\Gamma (\nabla \times \overline{\Phi}(x,x_q)q \times \nu, \Phi(x,x_p)p) - (\nabla \times \Phi(x,x_p)p \times \nu, \overline{\Phi}(x,x_q)q) ds = -2\mathrm{i}(p, \Im(\Phi(x_p,x_q))q). \tag{8}$$

Proof. It is easy to verify directly that the identify $(\nabla \times \nabla \times \Phi(x,x_p))p = \nabla \times \nabla \times \Phi(x,x_p)p$ holds for any constant vector $p \in \mathbb{C}^{\mathrm{d}}$. Using this identity and (3) we have

$$\nabla \times \nabla \times \Phi(x,x_p)p - k^2 \Phi(x,x_p)p = \delta(x-x_p)p \quad \forall\, p \in \mathbb{C}^{\mathrm{d}}, \tag{9}$$

$$\nabla \times \nabla \times \Phi(x,x_q)q - k^2 \Phi(x,x_q)q = \delta(x-x_q)q \quad \forall\, q \in \mathbb{R}^{\mathrm{d}}. \tag{10}$$

Taking the conjugate of equation (10) yields

$$\nabla \times \nabla \times \overline{\Phi}(x, x_q)q - k^2 \overline{\Phi}(x, x_q)q = \delta(x - x_q)q. \tag{11}$$

By taking (real) inner products of equation (9) with $\overline{\Phi}(x, x_q)q$ and of equation (11) with $\Phi(x, x_p)p$, then subtracting the two identities, we arrive at

$$\begin{aligned} \int_{\Omega_\Gamma} \big\{ (\overline{\Phi}(x, x_q)q, \nabla \times \nabla \times \Phi(x, x_p)p) - (\Phi(x, x_p)p, \nabla \times \nabla \times \overline{\Phi}(x, x_q)q) \big\} dx \\ = (p, \overline{\Phi}(x_p, x_q)q) - (q, \Phi(x_p, x_q)p). \end{aligned} \tag{12}$$

Next we apply the following integration by parts formula

$$\begin{aligned} &\int_{\Omega_\Gamma} \big\{ (\overline{\Phi}(x, x_q)q, \nabla \times \nabla \times \Phi(x, x_p)p) - (\Phi(x, x_p)p, \nabla \times \nabla \times \overline{\Phi}(x, x_q)q) \big\} dx \\ &\qquad = \int_\Gamma (\nabla \times \overline{\Phi}(x, x_q)q \times \nu, \Phi(x, x_p)p) - (\nabla \times \Phi(x, x_p)p \times \nu, \overline{\Phi}(x, x_q)q) ds \end{aligned}$$

to the left hand side of (12) to obtain

$$\begin{aligned} \int_\Gamma (\nabla \times \overline{\Phi}(x, x_q)q \times \nu, \Phi(x, x_p)p) - (\nabla \times \Phi(x, x_p)p \times \nu, \overline{\Phi}(x, x_q)q) ds \\ = (p, \overline{\Phi}(x_p, x_q)q) - (q, \Phi(x_p, x_q)p). \end{aligned}$$

Now the real symmetry of the fundamental solution $\Phi(x, y)$ leads directly to the desired identity. □

Next, note that on a circular curve/spherical surface Γ, we can approximate the left hand side of identity (8) by means of the Silver-Müller radiation condition for the outgoing fundamental solution $\Phi(x, y)$ to the Maxwell system, i.e.,

$$\nabla \times \Phi(x, x_p)p \times \nu = \mathrm{i}k\Phi(x, x_p)p + \text{h.o.t.}$$

Thus we have the following approximations:

$$\begin{aligned} \nabla \times \Phi(x, x_p)p \times \nu &\approx \mathrm{i}k\Phi(x, x_p)p, \\ \nabla \times \overline{\Phi}(x, x_q)q \times \nu &\approx -\mathrm{i}k\overline{\Phi}(x, x_q)q, \end{aligned}$$

which are valid if the points x_p and x_q are far away from the boundary Γ. Consequently, we arrive at the following important approximate relation:

$$-\int_\Gamma \Big\{ (\mathrm{i}k\, \Phi(x, x_p)p, \overline{\Phi}(x, x_q)q) + (\mathrm{i}k\, \overline{\Phi}(x, x_q)q, \Phi(x, x_p)p) \Big\} ds \approx -2\mathrm{i}(p, \Im(\Phi(x_p, x_q))q).$$

Upon simplifying the relation, we arrived at the desired relation (7).

The relation (7) leads to an important observation: the inner product over the surface Γ

$$\langle \Phi(\cdot, x_p)p, \Phi(\cdot, x_q)q \rangle_{L^2(\Gamma)} = \int_\Gamma (\Phi(x, x_p)p, \overline{\Phi}(x, x_q)q) ds \tag{13}$$

can have a maximum if $x_p = x_q$ and decays to 0 as $|x_p - x_q|$ tends to ∞, in view of the decay property of the fundamental solution $\Phi(x, y)$, i.e., an approximate "orthogonality" relation.

With these two basic facts (6) and (7) at hand, now we consider a sampling domain $\widetilde{\Omega} \subset \Omega_\Gamma$ enclosing the scatterer support Ω, and divide it into a set of small elements $\{\tau_j\}$. Then by a rectangular quadrature rule, we arrive at the following discrete sum representation

$$E^s(x) = \int_{\widetilde{\Omega}} \Phi(x, y)J(y)dy \approx \sum_j \Phi(x, y_j)J(y_j)\,|\tau_j|, \tag{14}$$

where the point y_j lies within the jth element τ_j, and $|\tau_j|$ is the volume/area of the element τ_j. Since the induced electrical current J vanishes identically outside the support Ω, the summation in (14) is actually only over those elements that intersect with Ω. We point out that, in practice, the scatterer support Ω may consist of several disjoint subregions, each being occupied by one homogeneous physical medium. By elliptic regularity theory [13, 35], the induced current $J = \eta E$ is smooth in each subregion, and thus the approximation in (14) can be made arbitrarily accurate by refining the elements $\{\tau_j\}$. Nonetheless, we reiterate that the relation (14) is only to motivate our method, and it is not needed in the implementation. Physically, it can be interpreted as follows: the scattered field E^s at any point $x \in \Gamma$ is a weighted average of that due to point scatterers located at $\{y_j\}$ lying within the true scatterer Ω.

The relations (7) and (14) together indicate that for any sampling point $x_p \in \widetilde{\Omega}$ and any constant vector $q \in \mathbb{R}^{\mathrm{d}}$, there holds

$$\begin{aligned}\langle E^s, \Phi(\cdot, x_p)q\rangle_{L^2(\Gamma)} &\approx \left\langle \sum_j \Phi(\cdot, y_j)J(y_j)|\tau_j|, \Phi(\cdot, x_p)q \right\rangle_{L^2(\Gamma)} \\ &= \sum_j |\tau_j| \langle \Phi(\cdot, y_j)J(y_j), \Phi(\cdot, x_p)q\rangle_{L^2(\Gamma)} \\ &\approx k^{-1} \sum_j |\tau_j| (J(y_j), \Im(\Phi(x_p, y_j))q).\end{aligned} \tag{15}$$

The analysis in Section 3.2 indicates that the quantity $|\langle J(y_j), \Phi(\cdot, x_p)q\rangle|$ achieves its maximum magnitude for some probing polarization q when the sampling point x_p approaches the physical point scatterer y_j, and decays quickly when x_p moves away from y_j. Therefore the quantity $|\langle E^s, \Phi(\cdot, x_p)q\rangle|$ may act as an indicator function to the presence of scatterers, and equivalently provides an estimate of the scatterer support Ω. These observations lead us to the following index function:

$$\Psi(x_p; q) = \frac{|\langle E^s, \Phi(\cdot, x_p)q\rangle_{L^2(\Gamma)}|}{\|E^s\|_{L^2(\Gamma)} \|\Phi(\cdot, x_p)q\|_{L^2(\Gamma)}}, \quad \forall\, x_p \in \widetilde{\Omega}. \tag{16}$$

Here $\Phi(\cdot, x_p)q$ acts as a probe/detector for the scatterers. In principle, the choice of the polarization q in the index $\Psi(x_p; q)$ can be quite arbitrary. Naturally, it is expected that the choice of q will affect the probing capability of the function $\Phi(x, x_p)q$. The analysis in Section 3.2 below will shed insights into the probing mechanism and provide useful guidelines for the choice of q. In particular, the choice $q = p$, i.e., the polarization of the incident field E^i, works well in practice. We note that, apart from providing an estimate of the scatterer support, the index $\Psi(x_p; q)$ provides a likelihood distribution of the inhomogeneities in $\widetilde{\Omega}$, which up to a multiplicative constant may be used as an initial estimate for further refinement [23].

3.2 Analysis of the index function Ψ

In this part, we analyze the theoretical performance and the probing mechanism of the DSM by analytically and numerically studying the fundamental solution $\Phi(x, y)$ and the index Ψ for one single point scatterer. First, we recall the crucial role of the approximate relation (7): the fundamental solution $\Phi(x_p, x_q)$ is nearly singular, and assumes very large values for x_p close to x_q. More precisely, the extremal property of $\Im(\Phi(x_p, x_q))$ is the basis for accurate support detection. This observation is self evident for the scalar Helmholtz equation in view of the identity $\Im(G(x_p, x_q)) = \frac{1}{4} J_0(k|x_p - x_q|)$ (in two-dimension), where J_0 is the Bessel function of the first kind of order zero. However, for the Maxwell system, the fundamental solution $\Phi(x, y)$ contains multiple entries, and each exhibits drastically different behavior. So for different polarization q, the probing function $\Phi(x, x_p)q$, as well as the index function $\Psi(x_p; q)$, mixes the components together differently and the probing capability may differ considerably. Below we shall investigate more closely the properties of $\Phi(x, y)$ to shed light into $\Psi(x_p; q)$.

We begin with an important observation on the trace of the fundamental solution $\Phi(x, y)$.

Proposition 3.1. *For* $\mathrm{d} = 2, 3$*, the fundamental solution* $\Phi(x, y)$ *satisfies the following relation*

$$\operatorname{tr}(\Phi(x, y)) = (\mathrm{d} - 1)k^2 G(x, y). \tag{17}$$

Proof. Let us begin with the two-dimensional case, i.e., transverse electric mode, i.e., $E = (E_1, E_2, 0)^{\mathrm{t}}$ and $H = (0, 0, H_3)^{\mathrm{t}}$. Then the Maxwell system (1) should be understood as

$$\mathrm{i}\omega\mu_0 H_3 = (\nabla \times E)_3 = \frac{\partial E_2}{\partial x_1} - \frac{\partial E_1}{\partial x_2}, \quad -\mathrm{i}\omega\epsilon E = \nabla \times H = \left(\frac{\partial H_3}{\partial x_2}, -\frac{\partial H_3}{\partial x_1}, 0\right)^{\mathrm{t}}.$$

The fundamental solution $G(x, y)$ is given by $G(x, y) = \frac{\mathrm{i}}{4} H_0^{(1)}(k\,|x - y|)$. To evaluate the Hessian $D^2 G(x, y)$, we first recall the recursive relation for the derivative of Hankel functions [1]

$$\frac{d}{dz} H_n^{(1)}(z) = \frac{n H_n^{(1)}(z)}{z} - H_{n+1}^{(1)}(z).$$

Hence, by the chain rule and product rule, we deduce that

$$\frac{\partial^2}{\partial x_i \partial x_j} H_0^{(1)}(k|x - y|) = k^2 H_2^{(1)}(k|x - y|) \frac{(x-y)_i (x-y)_j}{|x-y|^2} - k \frac{1}{|x-y|} H_1^{(1)}(k|x - y|)\delta_{i,j},$$

where δ_{ij} is the Kronecker delta function. Consequently, the fundamental solution $\Phi(x, y)$ is given by

$$\Phi(x, y)_{i,j} = \frac{\mathrm{i}k^2}{4} \left[\left(H_0^{(1)}(k|x - y|) - \frac{H_1^{(1)}(k|x-y|)}{k|x-y|} \right) \delta_{i,j} + H_2^{(1)}(k|x - y|) \frac{(x-y)_i (x-y)_j}{|x-y|^2} \right].$$

Upon noting the recursive relation $\frac{2H_1^{(1)}(z)}{z} = H_0^{(1)}(z) + H_2^{(1)}(z)$ for Hankel functions [1], we deduce that the trace of the fundamental solution satisfies

$$\begin{aligned} \operatorname{tr}(\Phi(x, y)) &= \frac{\mathrm{i}k^2}{4} \left[2H_0^{(1)}(k|x - y|) - 2\frac{H_1^{(1)}(k|x-y|)}{k|x-y|} + H_2^{(1)}(k|x - y|) \right] \\ &= \frac{\mathrm{i}k^2}{4} H_0^{(1)}(k|x - y|) = k^2 G(x, y). \end{aligned}$$

Next we turn to the three-dimensional case, i.e., $G(x, y) = \frac{1}{4\pi} \frac{e^{\mathrm{i}k|x-y|}}{|x-y|}$. A direct calculation yields

$$\begin{aligned} \Phi(x, y)_{ij} =& G(k|x - y|) \left[k^2 \left(\delta_{ij} - \frac{(x-y)_i (x-y)_j}{|x-y|^2} \right) - \left(\delta_{i,j} - \frac{3(x-y)_i (x-y)_j}{|x-y|^2} \right) \frac{1}{|x-y|^2} \right. \\ &\left. + \mathrm{i}k \left(\delta_{i,j} - \frac{3(x-y)_i (x-y)_j}{|x-y|^2} \right) \frac{1}{|x-y|} \right]. \end{aligned}$$

Consequently, there holds $\operatorname{tr}(\Phi(x, y)) = 2k^2 G(x, y)$. This completes the proof. □

It follows from (17) that the sum of the diagonals of $\Phi(x, y)$ resembles the scalar counterpart $G(x, y)$, which, according to [22, 28], can detect well the scatterer support. In other words, this yields

$$k^{-1} \Im(\operatorname{tr} \Phi(x, y)) = \begin{cases} \dfrac{k^2}{4} \dfrac{J_0(k|x - y|)}{k}, & \mathrm{d} = 2, \\ 2k^2 \dfrac{\sin(k|x - y|)}{k|x - y|}, & \mathrm{d} = 3. \end{cases} \tag{18}$$

Therefore, the crucial quantity $k^{-1}\Im(\operatorname{tr}(\Phi(x_p, x_q)))$ attains its maximum at $x_p = x_q$, indicating the presence of a scatterer. We note that apart from the global maximum, there are also a number of local maxima, which introduce "ripples" into the resulting index function. Nonetheless, the locations of these maxima depend only on the wavenumber k, and can be strictly calibrated.

Next, we examine combinations of the components of the fundamental solution $\Phi(x, y)$. We first note that each independent component $\Im(\Phi_{ij}(x, x_q))$ does have a significant maximum at $x = x_q$ like (18). However, the magnitude of each component differs dramatically. In Fig. 1, we show the inner products

of the components Φ_{11}, Φ_{22}, Φ_{12} with themselves (termed cross product for short) and the diagonal sum as a function of the sampling point $x_p \in \widetilde{\Omega}$, i.e., $|\langle \Phi_{11}(x_p, x), \Phi_{11}(x_q, x)_{L^2(\Gamma)} \rangle|$ etc. We note that these cross products form the building blocks of the index function $\Psi(x_p; q)$, and their behavior completely determines the performance of the DSM. The cross products for both Φ_{11} and Φ_{22} exhibit strong directional resonances but their sum, i.e., $\langle \Phi_{11}(x, x_q), \Phi_{11}(x, x_p) \rangle_{L^2(\Gamma)} + \langle \Phi_{22}(x, x_q), \Phi_{22}(x, x_p) \rangle_{L^2(\Gamma)}$ does only assume one significant maximum at $x_q = x_p$ with weak resonances. In practice, due to the mixing of these components in $\Psi(x_p; q)$, the performance of the DSM may not be as good as that for the scalar counterpart in the case of the scattered electric field E^s for one polarization. Nonetheless, with multiple polarizations p_k and all components of the respective scattered field E^s, one might be able to extract the trace $\mathrm{tr}(\Phi(x, y))$, and (18) can be applied. If this were indeed the case, then the performance of the sampling method would equal that for the scalar case.

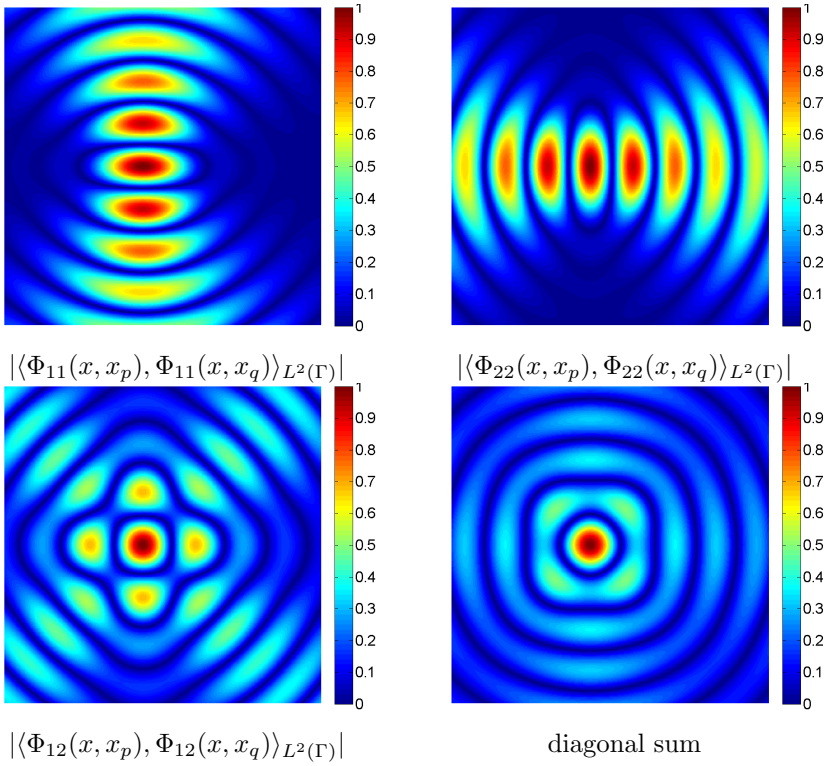

Figure 1: Cross products of Φ_{11}, Φ_{22}, and Φ_{12}, with the point scatterer located at the $x_q = (-\frac{1}{4}, 0)$, and the diagonal sum, over the sampling domain $\widetilde{\Omega} = [-2, 2]^2$. The measurement curve Γ is a circle of radius 5 centered at the origin. The quantities are normalized.

Index function for multiple incident fields. To arrive at an applicable index function for multiple incident fields (with different incident directions/polarizations), we examine the behavior of the two-dimensional fundamental solution $\Phi(x, y)$ more closely. We first consider the incident direction $d_1 = \frac{\sqrt{2}}{2}(1, 1)^{\mathrm{t}}$ and the polarization $p_1 = \frac{\sqrt{2}}{2}(1, -1)^{\mathrm{t}}$, and assume that the local induced electrical current J is proportional to the polarized incident wave E^i within the inhomogeneity located at x_q. Upon ignoring the normalization, the index function $\Psi(x_p; q)$ with the choice $q = p_1$ is roughly determined by

$$\begin{aligned} 2\langle \Phi(x, x_q)p_1, \Phi(x, x_p)p_1 \rangle_{L^2(\Gamma)} =& \langle \Phi_{11}(x, x_q) - \Phi_{12}(x, x_q), \Phi_{11}(x, x_p) - \Phi_{12}(x, x_p) \rangle_{L^2(\Gamma)} \\ &+ \langle \Phi_{12}(x, x_q) - \Phi_{22}(x, x_q), \Phi_{12}(x, x_p) - \Phi_{22}(x, x_p) \rangle_{L^2(\Gamma)}, \end{aligned}$$

where each term in the inner products, like $\Phi_{11}(x,x_p)-\Phi_{12}(x,x_q)$ and so on, corresponds to one component of the vector field E^s. Similarly, for the incident direction $d_2=\frac{\sqrt{2}}{2}(1,-1)^{\mathrm{t}}$ and the polarization $p_2=\frac{\sqrt{2}}{2}(1,1)^{\mathrm{t}}$, the index function $\Phi(x_p;q)$ with the choice $q=p_2$ is roughly determined by

$$\begin{aligned}2\langle\Phi(x,x_q)p_2,\Phi(x,x_p)p_2\rangle_{L^2(\Gamma)}=&\langle\Phi_{11}(x,x_q)+\Phi_{12}(x,x_q),\Phi_{11}(x,x_p)+\Phi_{12}(x,x_p)\rangle_{L^2(\Gamma)}\\&+\langle\Phi_{12}(x,x_q)+\Phi_{22}(x,x_q),\Phi_{12}(x,x_p)+\Phi_{22}(x,x_p)\rangle_{L^2(\Gamma)}.\end{aligned}$$

The quantities $|\langle\Phi(x,x_q)p_1,\Phi(x,x_p)p_1\rangle_{L^2(\Gamma)}|$ and $|\langle\Phi(x,x_q)p_2,\Phi(x,x_p)p_2\rangle_{L^2(\Gamma)}|$ after normalization are shown in Fig. 2: both exhibit strong resonances. This is attributed to the ripples predicted from the relation (18) and mixing of different components of Φ. Note that the resonances show up in different regions, with their locations depending on the incident direction/polarization. We reiterate that in case of one single point scatterer, the resonance is completely predictable and one might be able to remove them from the support estimates with suitable postprocessing. However, for multiple scatterers, the discrimination of resonances from true scatterers can be highly nontrivial. Hence, it is highly desirable to design a sampling method that is free from significant resonances ab initio, by suitably adapting the choice of polarization q in the probing function $\Phi(x,x_p)q$ and combining the indices for multiple polarizations. Let us consider two polarizations $p_1=\frac{\sqrt{2}}{2}(1,-1)^{\mathrm{t}}$ and $p_2=\frac{\sqrt{2}}{2}(1,1)^{\mathrm{t}}$, and measure all components of the scattered electric field E^s, in the hope of focusing on the genuine inhomogeneities. Then the performance of the combined index with $p_1=\frac{\sqrt{2}}{2}(1,-1)^{\mathrm{t}}$ and $p_2=\frac{\sqrt{2}}{2}(1,1)^{\mathrm{t}}$ is approximately given by

$$\begin{aligned}&\langle\Phi(x,x_q)p_1,\Phi(x,x_p)p_1\rangle_{L^2(\Gamma)}+\langle\Phi(x,x_q)p_2,\Phi(x,x_p)p_2\rangle_{L^2(\Gamma)}\\=&\langle\Phi_{11}(x,x_q),\Phi_{11}(x,x_p)\rangle_{L^2(\Gamma)}+2\langle\Phi_{12}(x,x_q),\Phi_{12}(x,x_p)\rangle_{L^2(\Gamma)}+\langle\Phi_{22}(x,x_q),\Phi_{22}(x,x_p)\rangle_{L^2(\Gamma)}.\end{aligned}$$

Even though the index function for p_1 or p_2 alone has its own shadows of the point scatterer; see Figs. 2(a)-(b); the combination can isolate the point scatterer very well, cf. Fig. 2(c). Hence, combining multiple polarizations does remedy the undesirable rippling phenomenon. This motivates the following combined index $\Psi_c(x_p)$ for multiple polarizations $\{p_l\}_{l=1}^L$:

$$\Psi_c(x_p)=\frac{1}{L}\sum_{l=1}^{L}\Psi(x_p;p_l) \tag{19}$$

where $\Psi(x_p;p_l)$ is the index function for the polarization p_l (hence the lth incident field), cf. (16).

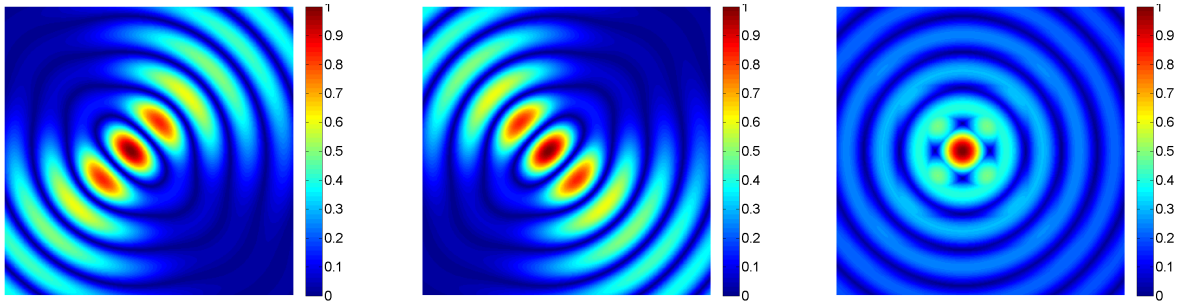

(a) $|\langle\Phi(x,x_p)p_1,\Phi(x,x_q)p_1\rangle_{L^2(\Gamma)}|$ (b) $|\langle\Phi(x,x_p)p_2,\Phi(x,x_q)p_2\rangle_{L^2(\Gamma)}|$ (c) combination

Figure 2: The cross products for polarizations p_1, p_2 and the combination with direct sum over the sampling domain $\widetilde{\Omega}=[-2,2]^2$. The point scatterer is located at $x_q=(-\frac{1}{4},0)$. The measurement curve Γ is a circle of radius 5 centered at the origin. The quantities are normalized.

3.3 Comparisons with existing methods

There are several existing sampling-type methods for inverse scattering, including linear sampling method (LSM), factorization method [24, 25], MUSIC [16, 4, 9], and orthogonality sampling etc; see [8, 10, 24,

25, 29] for detailed overviews on these methods. In this subsection, we briefly discuss the connections and differences between the DSM and the LSM and MUSIC.

The LSM was introduced in 1996 [12]. Numerically, for each sampling point, it solves one linear integral equation of the first kind with the measured far-field data as the kernel, and then takes the solution norm as an indicator function. Hence, the LSM takes the far-field map, and involves solving linear ill-posed integral equations, which necessitates the application of regularization methods. In comparison with optimization-based indirect methods, it is much faster. Further, with a full range of scattered field data, the reconstructions are generally accurate, but a full range may not be required for the method to yield a (sometimes reasonable) result. However, the data noise is treated indirectly via linear solvers, thus the value of the indicator function is usually sensitive to the noise. We refer to [11, 8] for overviews on the LSM for inverse electromagnetic scattering problems. In contrast, as we shall see below, the DSM can work with a few incident fields, and treats directly the data noise.

In inverse scattering, MUSIC was often applied to retrieve the locations of point-like scatterers from the multistatic response (MSR) matrix; see, e.g., [4, 16] for acoustic scattering, and [5, 9] for electromagnetic scattering. Numerically, it involves projecting test functions $\Phi(x, x_p)q$ into a noise subspace, which is computed by the eigendecomposition of the MSR matrix. We note that for one incident field and a point-like scatterer, the indicator functions for the DSM and MUSIC are very similar, which roughly are the cosine and cosecant of the angle between the scattered field and the test function, respectively. This underlies their close connection. Nonetheless, there are several notable differences in their motivation, derivation and implementation. First, by the MSR matrix, MUSIC generally requires multiple incident fields, but the DSM uses very few (e.g., one or two) incidents. Further, we note that for the case of one incident field, the interpretation of the index function developed herein is new, i.e., crucial roles of the relations (6) and (7). Second, the derivation of MUSIC ignores multiple scattering [25], whereas the DSM is based on a scattering analysis and accommodates multiple scattering. Third, MUSIC is based on a range condition and aims mainly at point scatterers, whereas the DSM relies on formula (15) of the probing function and profiles the distributed induced current of the scatterers, which are not necessarily point-like. Fourth, MUSIC requires computing the noise subspace, which is relatively sensitive to the presence of noise. In the DSM, noisy data enters into the index function (16) directly via the integral over the surface Γ against the fundamental solution. By the smoothness of the fundamental solution, the high frequency modes (noise) in the data are less influential; see the numerical experiments in Section 4. Last, in case of multiple incidents, the DSM first forms one index function for each incident, and then sum them up to yield the combined index Ψ_c, to enhance the probing effect based on the analysis in Section 3.2. This is distinctly different from MUSIC, where the scattered data is first combined into a signal subspace, and it represents one of the main novelties of the DSM. Further, MUSIC generally uses one fixed but possibly space dependent polarization in the test function $\Phi(x, x_p)q$, which can limit its probing capability. The reconstruction quality depends crucially on the choice of the polarization q, and an inadvertent choice may miss degenerate scatterers [3, 9]. In contrast, in the DSM, one can adapt the polarization in the probing function $\Phi(x, x_p)q$ to each incident field, then sum the indices together for an improved reconstruction resolution. Altogether, these differences essentially distinguish the DSM from the standard MUSIC.

Now we summarize the distinct features of the DSM. First, it involves only computing inner products of the measured scattered field with closed-form probing functions $\Phi(x, x_p)q$, hence it is strictly direct. Second, it is applicable to the case of a few (e.g., one or two) incident fields, which is particularly important in applications. Surely with such a limited amount of data, the reconstruction accuracy has to be somewhat compromised in comparison with that from a full range of scattered fields. However, as we shall see below, the reconstructions are still reasonable. Third, the noise is treated directly, thus the method is usually robust with respect to the noise.

4 Numerical experiments and discussions

In this section, we present two- and three-dimensional numerical examples to showcase the features, e.g., the accuracy and robustness, of the proposed DSM for detecting scatterers. The examples are designed to illustrate the features of the method and to validate the theoretical findings in Section 3. Numerical results for both exact and noisy data will be presented. In all examples, the wavelength λ is set to 1, and the wavenumber k is 2π. The noisy scattered electric data E^s_δ is generated pointwise by

$$E^s_\delta(x) = E^s(x) + \varepsilon \max_{x\in\Gamma} |E^s(x)|\zeta(x),$$

where ε denotes the relative noise level, and both real and imaginary parts of the random variable $\zeta(x)$ follow the standard Gaussian distribution with zero mean and unit variance. All the computations were performed on a dual-core laptop using `MATLAB` R2009a.

4.1 Two-dimensional examples

Now we present numerical results for two-dimensional examples. Unless otherwise specified, two incident fields, i.e., $d_1 = \frac{\sqrt{2}}{2}(1,1)^{\mathrm{t}}$ and $d_2 = \frac{\sqrt{2}}{2}(-1,1)^{\mathrm{t}}$ (accordingly, the polarizations $p_1 = \frac{\sqrt{2}}{2}(1,-1)^{\mathrm{t}}$ and $p_2 = \frac{\sqrt{2}}{2}(1,1)^{\mathrm{t}}$), are employed. For each incident field E^i, the scattered electric field E^s is measured at 30 points uniformly distributed on a circle of radius 5 centered at the origin. The sampling domain $\widetilde{\Omega}$ is fixed at $[-2,2]^2$, which is divided into small squares of equal side length $h = 0.01$. The index function Ψ as an estimate to the scatterer support will be displayed for each example.

Our first example shows the method for one single scatterer, which confirms the theoretical analysis of the index Ψ_c in Section 3.2.

Example 1. *The example considers one square scatterer of side length* 0.3 *centered at the point* $(-\frac{1}{4}, 0)$. *The true inhomogeneity coefficient* $\eta(x)$ *of the scatterer is set to be* 1, *namely* $n(x) = \sqrt{2}$.

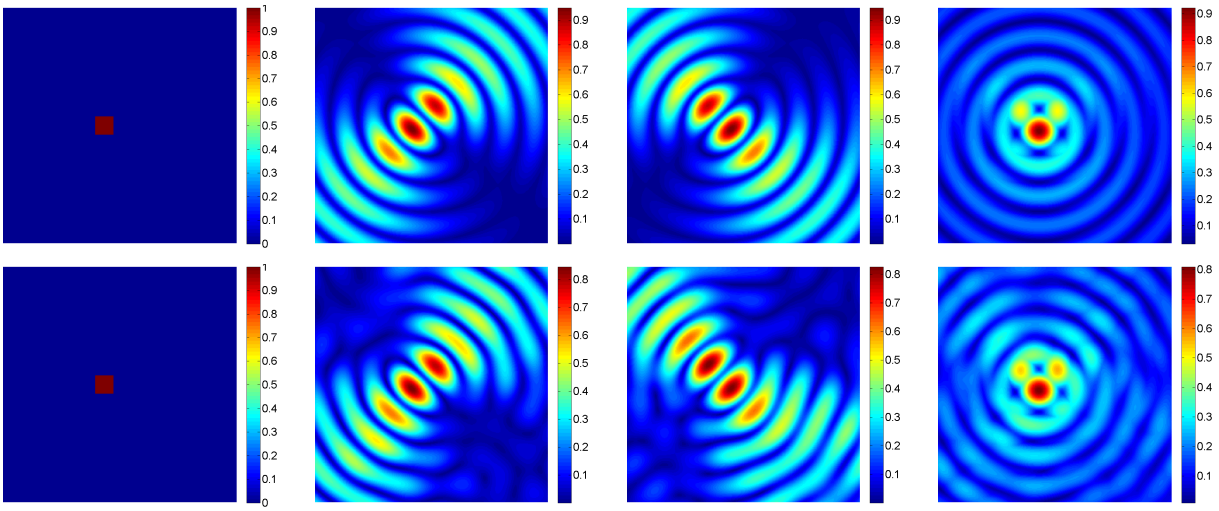

(a) true scatterer (b) index $\Psi(x_p; p_1)$ (c) index $\Psi(x_p; p_2)$ (d) index Ψ_c

Figure 3: Numerical results for Example 1. The first and second row refers respectively to the index function for the exact data and the noisy data with $\varepsilon = 20\%$ noise.

The numerical results for Example 1 are shown in Fig. 3. We observe that for sampling points close to the physical scatterer, the index function Ψ is relatively large; otherwise it takes relatively small values. Note that the image for one incident field E^i exhibits obvious resonances, with resonance locations

depending on the incident direction. Here, the resonance behavior agrees excellently with the theoretical analysis for one single point scatterer in Section 3.2, hence it might be removed by applying a suitable postprocessing procedure. The use of two incident fields can greatly mitigate the resonances. Hence the index function Ψ_c does provide an accurate and reliable indicator for the location of the scatterer; see Fig. 3(d). The presence of $\varepsilon = 20\%$ noise in the measured data does not affect the shape of Ψ_c, thereby showing the robustness of the DSM.

Our second example illustrates the DSM for two separate scatterers.

Example 2. *We consider two square scatterers, with the inhomogeneity coefficient η being 1 in both scatterers. The following two cases are investigated:*

(a) The two scatterers are of side length 0.2, and located at $(-0.8, -0.7)$ and $(0.3, 0.8)$, respectively.

(b) The two scatterers are of side length 0.3, and located at $(-0.45, -0.35)$ and $(0.05, 0.15)$, respectively.

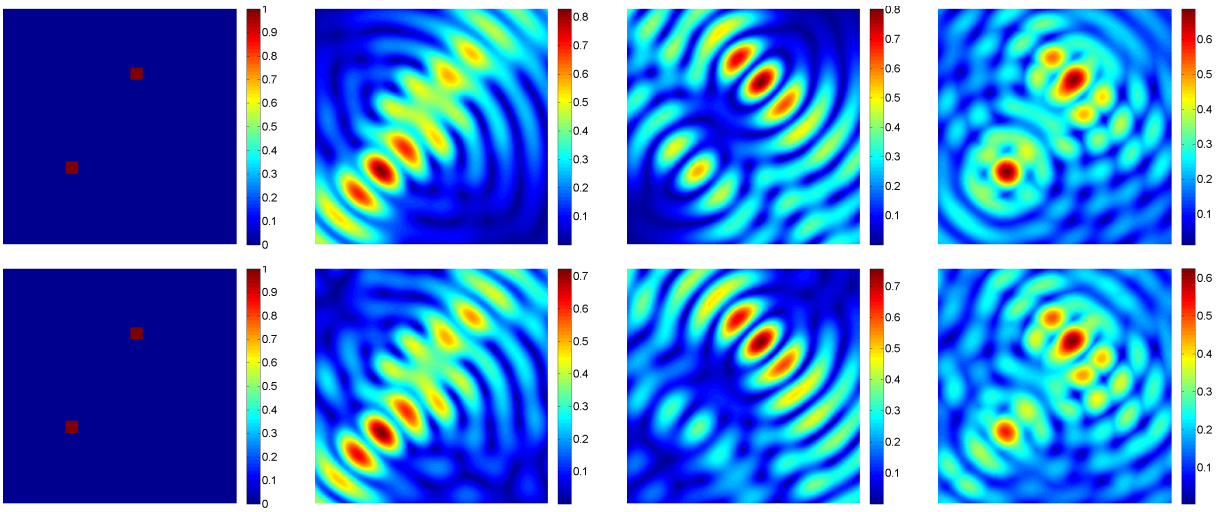

(a) true scatterers (b) index $\Psi(x_p; p_1)$ (c) index $\Psi(x_p; p_2)$ (d) index Ψ_c

Figure 4: Numerical results for Example 2(a). The first and second row refers respectively to the index function for the exact data and the noisy data with $\epsilon = 20\%$ noise.

The two scatterers in Example 2(a) are well apart from each other. Here each of the two incident fields tends to highlight only one of the two scatterers, with the index value for one scatterer being much higher than that for the other; see Figs. 4(b)-(c). Since the two scatterers are well apart, the interactions between them are weak, and the resonance pattern for the point scatterer is well kept. However, the two incident fields together give a clear discrimination of the two scatterers, with their locations satisfactorily recovered for both exact data and the data with $\epsilon = 20\%$ noise; see Fig. 4(d).

The two scatterers in Example 2(b) stay very close to each other. We observe that, for the incident direction d_2, apart from the strong resonances, the locations for the scatterers cannot be directly inferred since the index function Ψ relates the two scatterers into an elongated ellipse shape. The resonances were almost completely removed from the estimate when using two incident fields. Hence the estimate of the locations of the scatterers is very impressive: the two scatterers are still well separated despite their closeness, with their locations correctly estimated, for up to $\epsilon = 20\%$ noise in the data. Although not presented, we would like to remark that in the case of very high noise levels, e.g., $\epsilon = 40\%$, the estimate tends to connect the two scatterers, and also some spurious modes may emerge.

Our next example considers the more challenging case of three neighboring scatterers.

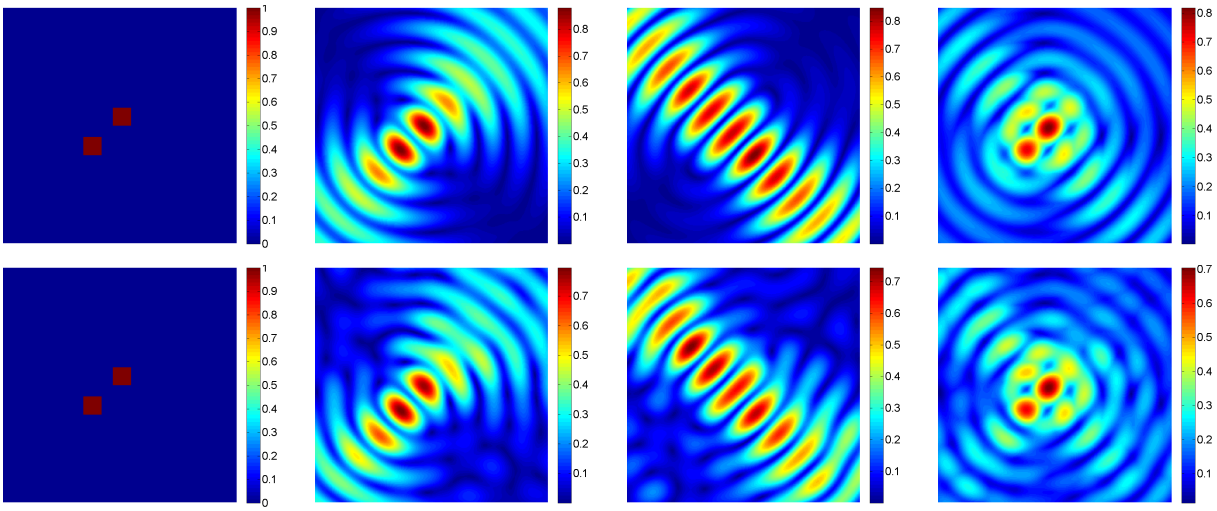

(a) true scatterers (b) index $\Psi(x_p; p_1)$ (c) index $\Psi(x_p; p_2)$ (d) index Ψ_c

Figure 5: Numerical results for Example 2(b). The first and second row refers respectively to the index function for the exact data and the noisy data with $\epsilon = 20\%$ noise.

Example 3. *This example consists of three neighboring square scatterers of width* 0.15*: one located at* $(-\frac{5}{8}, -\frac{5}{8})$*, one located at* $(-\frac{17}{40}, -\frac{17}{40})$*, and one located at* $(-\frac{21}{40}, \frac{1}{8})$*. The inhomogeneity coefficients of all three scatterers are set to be* $\eta = 1$*.*

In this example, the three scatterers stay very close to each other, especially the upper two, thus it is numerically very challenging to separate them. This is also reflected in the fact that each individual incident field tends to combine two of the three scatterers into one larger chunk, which is true for both the exact data and noisy data; see Figs. 6 (b)-(c). Thus it is difficult to tell from either Fig. 6(b) or Fig. 6(c) the number and locations of the scatterers. The latter is effectively remedied by using two incident fields together; see Fig. 6(d), where the scatterers are vividly separated from each other. However, the interactions between the scatterers focus the strength on the scatterer to the right, and diminish slightly the strength of the scatterer to the left.

Next we consider a ring-shaped scatterer.

Example 4. *This scatterer is one ring-shaped square scatterer located at the origin, with the outer and inner side lengths being* 0.6 *and* 0.4*, respectively. The coefficient* η *of the scatterer is* 1*.*

The ring-shaped scatterer represents one of the most challenging objects to resolve, and it is highly nontrivial even with multiple data sets. The results with the exact data and $\epsilon = 20\%$ noise in the data are shown in Fig. 7. It is observed that with just two incident waves, the method can provide a quite reasonable estimate of the ring shape, and it remains very stable for up to $\epsilon = 20\%$ noise in the data.

4.2 Three-dimensional example

The last example shows the feasibility of the method for three-dimensional problems.

Example 5. *We consider two cubic scatterers with side length* 0.2*: one centered at* $(0.4, 0.3, 0.3)$ *and the other at* $(-0.4, 0.3, 0.3)$*, respectively, and the coefficient* η *in both scatterers is taken to be* 1*.*

Here we take two incident fields, with the incident directions $d_1 = d_2 = \frac{1}{\sqrt{3}}(1, 1, 1)^{\mathrm{t}}$ and the polarization vectors $p_1 = \frac{1}{\sqrt{6}}(1, -2, 1)^{\mathrm{t}}$ and $p_2 = \frac{1}{\sqrt{6}}(1, 1, -2)^{\mathrm{t}}$. The scattered field E^s is measured at the points on a uniformly distributed mesh of 10×10 on each face of the cube of edge length 10. The sampling

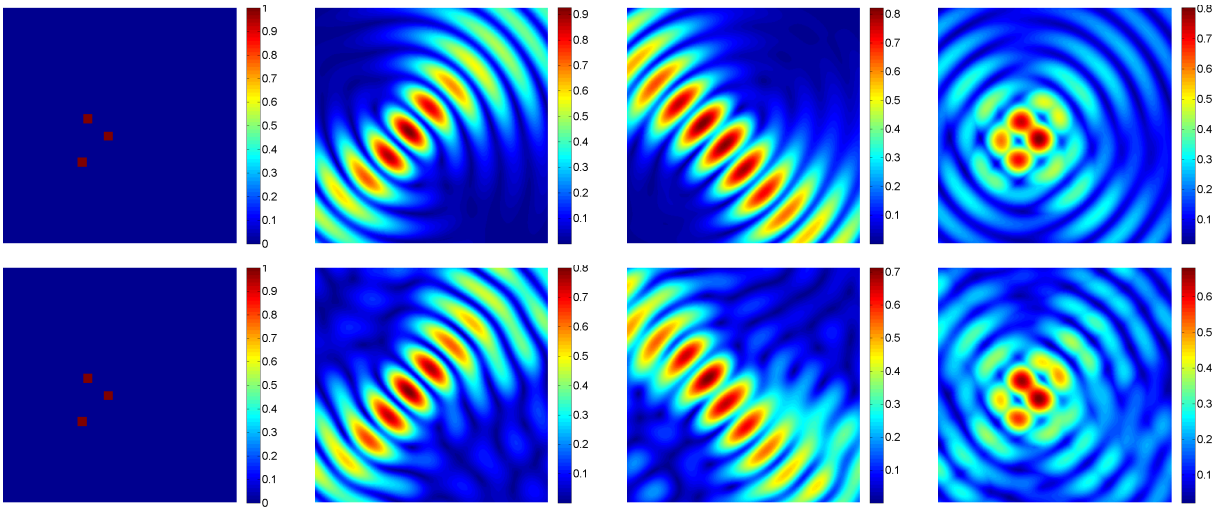

(a) true scatterers (b) index $\Psi(x_p; p_1)$ (c) index $\Psi(x_p; p_2)$ (d) index Ψ_c

Figure 6: Numerical results for Example 3. The first and second row refer to the index function for the exact data and the noisy data with $\epsilon = 20\%$ noise.

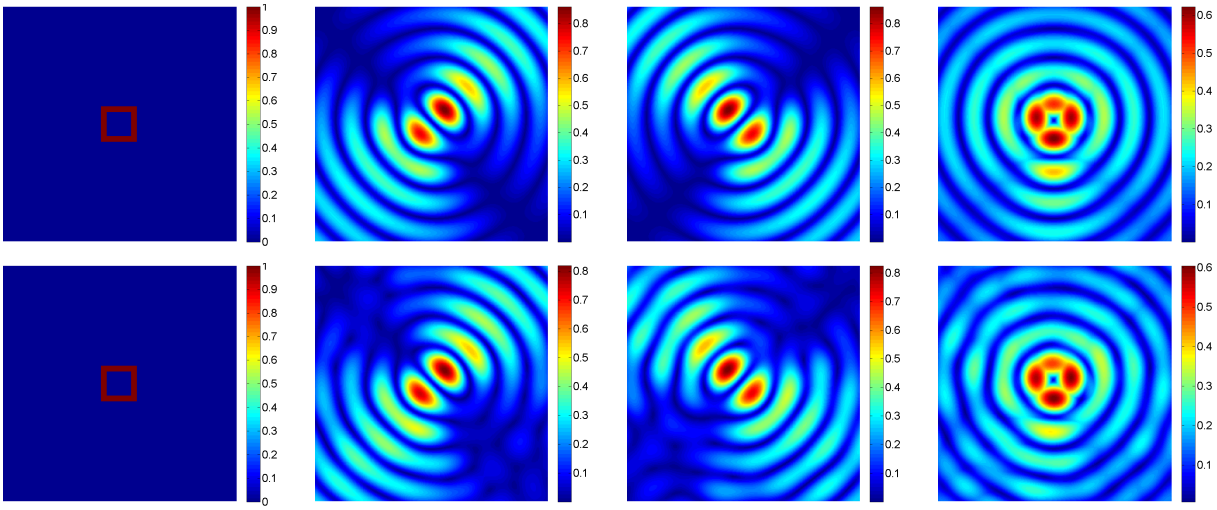

(a) true scatterers (b) index $\Psi(x_p; p_1)$ (c) index $\Psi(x_p; p_2)$ (d) index Ψ_c

Figure 7: Numerical results for Example 4. The first and second row refers respectively to the index function for the exact data and the noisy data with $\epsilon = 20\%$ noise.

domain $\widetilde{\Omega}$ for evaluating the index functions is taken to be $[-2, 2]^3$. The problem is discretized with a mesh size 0.02. The numerical results are shown in Fig. 8. We observe that the support estimated by the index Ψ agrees very well with the exact one, the magnitude of the index Ψ decreases quickly away from the boundary of the true scatterers. The presence of $\epsilon = 20\%$ data noise (cf. Fig. 9) seems to cause no obvious deterioration of the accuracy of the index Ψ when compared with that for the exact data. By examining the cross-sectional images of the index, we found that in comparison with two-dimensional problems, the rippling phenomenon seems far less pronounced for this three-dimensional example, i.e., one incident field is sufficient for the DSM to yield a reasonable scatterer support estimate.

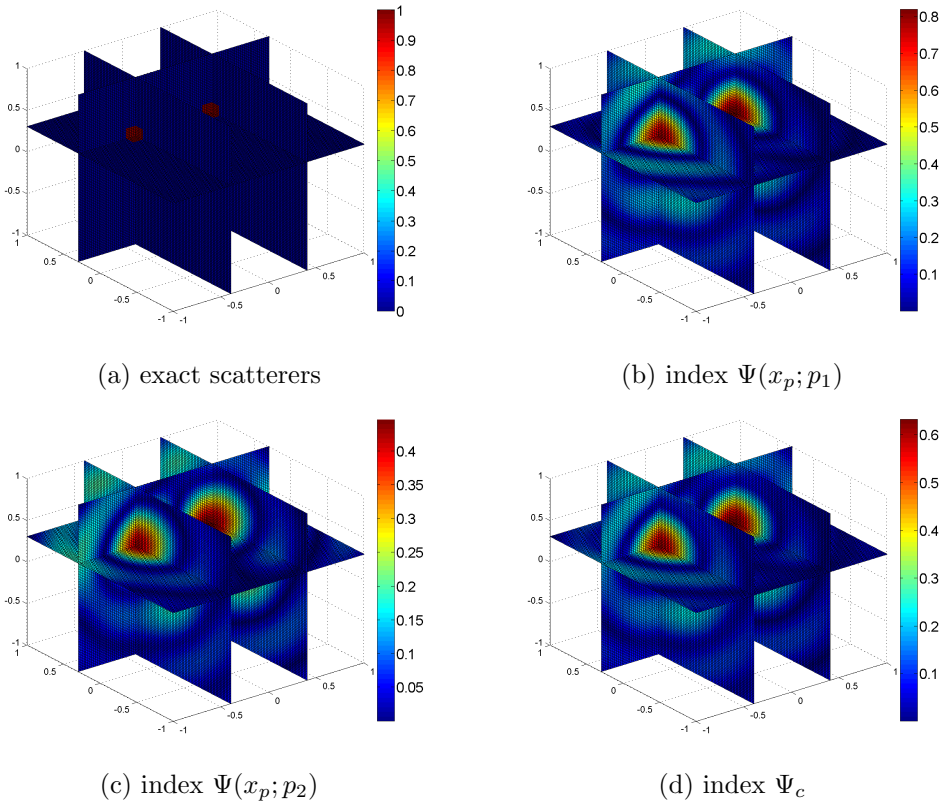

(a) exact scatterers

(b) index $\Psi(x_p; p_1)$

(c) index $\Psi(x_p; p_2)$

(d) index Ψ_c

Figure 8: Numerical results for Example 5 with exact data.

5 Conclusions

We have developed a novel direct sampling method for the inverse electromagnetic medium scattering problem of estimating the support of inhomogeneities from near-field scattered electric data. It was derived from an integral representation of the scattered field via the fundamental solution, a careful analysis on electromagnetic scattering and the behavior of the fundamental solution. It is particularly suited to the case of a few incident fields. It involves only computing inner products of the scattered electric field with fundamental solutions located at the sampling points, hence it is strictly direct, straightforward to implement, computationally very efficient, and very robust to noise presence. The numerical results indicate that it can provide satisfactory estimates of the scatterer shapes from the measured near-field data for a few incident fields, even in the presence of a large amount of noise in the data.

In the present study, we have focused on scatterer support estimation. It is natural to enhance the reconstructions by other indirect inverse scattering methods [23]. Also it is of interest to see its extensions for other important scattering scenarios, e.g., scattering from lines (cracks), far-field measurements and multiple-frequency data, as well as their theoretical justifications.

Acknowledgements

The authors would like to thank the anonymous referees and the board member for helpful comments, which have significantly improved the quality of the paper. The work of KI was partially supported by the Army Research Office under DAAD19-02-1-0394, US-ARO grant 49308-MA, and US-AFSOR grant FA9550-06-1-0241, that of BJ was supported by award KUS-C1-016-04, made by King Abdullah

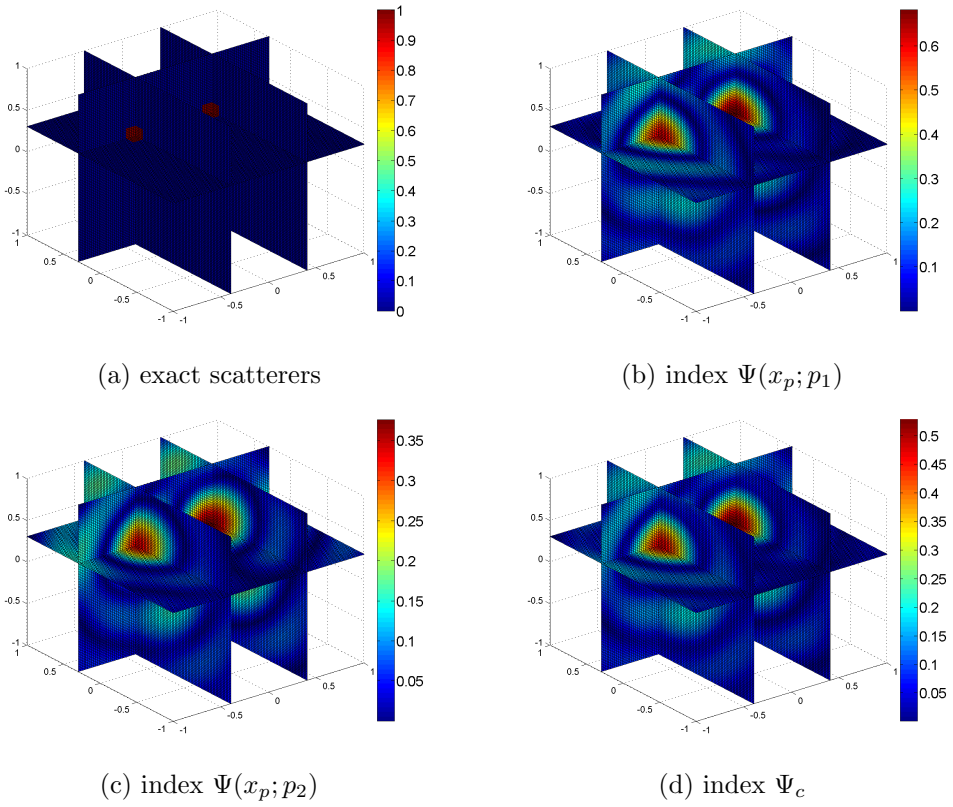

(a) exact scatterers

(b) index $\Psi(x_p; p_1)$

(c) index $\Psi(x_p; p_2)$

(d) index Ψ_c

Figure 9: Numerical results for Example 5 with $\epsilon = 20\%$ data noise.

University of Science and Technology (KAUST), and that of JZ was substantially supported by Hong Kong RGC grants (projects 405110 and 404611).

A Numerical method for forward scattering

In this part we describe our numerical method for the integral equation (5) on a two-dimensional domain Ω. We denote by $\mathbb{J}$ the index set of grid points $x_j = (x^1_{j_1}, x^2_{j_2})$, $j = (j_1, j_2) \in \mathbb{J}$, of a uniformly distributed mesh with a mesh size $h > 0$ and the square cells B_j given by

$$B_j = B_{j_1,j_2} = (x^1_{j_1}, x^2_{j_2}) + [-\tfrac{h}{2}, \tfrac{h}{2}] \times [-\tfrac{h}{2}, \tfrac{h}{2}]$$

for every tuple $j = (j_1, j_2)$ in the index set $\mathbb{J}$. Further, we assume that the set $\cup_{j\in\mathbb{J}} B_j$ contains the scatterer support Ω. We shall approximate the integral equation (5) by a mid-point quadrature rule, i.e.,

$$J_k + \eta_k \sum_{j\in\mathbb{J}} G_{k,j}(PJ)_j h^2 = \eta_k\, E^i(x_k), \quad k \in \mathbb{J}, \tag{20}$$

where $J_k = J(x_k)$ and $\eta_k = \eta(x_k)$, and the off-diagonal entries $G_{k,j}$ and the diagonal entries $G_{k,k}$ are given by $G_{k,j} = G(x_k, x_j)$ and $G_{k,k} = \frac{1}{h^2}\int_{(-\frac{h}{2},\frac{h}{2})^2} G(x, 0)dx$, respectively. The diagonal entries $G_{k,k}$ can be accurately computed by a tensor-product Gaussian quadrature rule. To arrive at a fully discrete scheme, we further approximate the crucial term PJ in equation (20) by the central finite difference scheme:

$$PJ = k^2 \begin{pmatrix} J & \\ & J \end{pmatrix} + \begin{pmatrix} D_{x_1x_1} & D_{x_1x_2} \\ D_{x_1x_2} & D_{x_2x_2} \end{pmatrix} J,$$

where $D_{x_ix_j}$ refers to taking the second-order derivative with respect to x_i and x_j. In practice, we shall approximate $D_{x_ix_j}$ by central finite difference scheme, i.e.,

$$D_{x_1x_1} = H \otimes I, \quad D_{x_2x_2} = I \otimes H, \quad D_{x_1x_2} = D \otimes D,$$

where $\otimes$ is the Kronecker product for matrices, H and D are the tridiagonal matrices for the second and the first derivative, respectively. The extension of the method to 3D problems is straightforward. The resulting system can be solved using standard linear solvers, e.g., Gaussian elimination, if the cardinality of the index set $\mathbb{J}$ is medium. Iterative solvers, e.g., generalized minimal residual method (GMRES) [31] should be applied if the cardinality of $\mathbb{J}$ is large. Our numerical experiences indicate that tens of GMRES iterations already yield a very accurate solution to the linear system.

References

[1] M. Abramowitz and I. A. Stegun. *Handbook of Mathematical Functions with Formulas, Graphs, and Mathematical Tables*. Govt. Print. Off., Washington, 1968.

[2] A. Abubakar, T. M. Habashy, P. M. van den Berg, and D. Gisolf. The diagonalized contrast source approach: an inversion method beyond the Born approximation. *Inverse Problems*, 21(2):685–702, 2005.

[3] K. Agarwal and X. Chen. Applicability of music-type imaging in two-dimensional electromagnetic inverse problems. *IEEE Trans. Ant. Prop.*, 56(10):3217–3223, 2008.

[4] H. Ammari, E. Iakovleva, and D. Lesselier. A MUSIC algorithm for locating small inclusions buried in a half-space from the scattering amplitude at a fixed frequency. *Multiscale Model. Simul.*, 3(3):597–628, 2005.

[5] H. Ammari, E. Iakovleva, D. Lesselier, and G. Perrusson. MUSIC-type electromagnetic imaging of a collection of small three-dimensional inclusions. *SIAM J. Sci. Comput.*, 29(2):674–709, 2007.

[6] G. Bao and P. Li. Inverse medium scattering problems for electromagnetic waves. *SIAM J. Appl. Math.*, 65(6):2049–2066, 2005.

[7] A. E. Bulyshev, A. E. Souvorov, S. Y. Semenov, V. G. Posukh, and Y. E. Sizov. Three-dimensional vector microwave tomography: theory and computational experiments. *Inverse Problems*, 20(4):1239–1259, 2004.

[8] F. Cakoni, D. Colton, and P. Monk. *The Linear Sampling Method in Inverse Electromagnetic Scattering*. SIAM, 2011.

[9] X. Chen and Y. Zhong. MUSIC electromagnetic imaging with enhanced resolution for small inclusions. *Inverse Problems*, 25(1):015008, 12, 2009.

[10] M. Cheney. The linear sampling method and the MUSIC algorithm. *Inverse Problems*, 17(4):591–595, 2001.

[11] D. Colton, H. Haddar, and M. Piana. The linear sampling method in inverse electromagnetic scattering theory. *Inverse Problems*, 19(6):S105–S137, 2003.

[12] D. Colton and A. Kirsch. A simple method for solving inverse scattering problems in the resonance region. *Inverse Problems*, 12(4):383–393, 1996.

[13] D. Colton and R. Kress. *Inverse Acoustic and Electromagnetic Scattering Theory*. Springer-Verlag, Berlin, 2 edition, 1998.

[14] T. J. Cui, W. C. Chew, A. A. Aydiner, and S. Chen. Inverse scattering of two-dimensional dielectric objects buried in a lossy earth using the distorted Born iterative method. *IEEE Trans. Geosci. Rem. Sens.*, 39(2):339–346, 2001.

[15] J. De Zaeytijd, A. Franchois, C. Eyraud, and J.-M. Geffrin. Full-wave three-dimensional microwave imaging with a regularized Gauss-Newton method - theory and experiment. *IEEE Trans. Antenn. Prop.*, 55(11):3279–3292, 2007.

[16] A. J. Devaney. Super-resolution processing of multi-static data using time-reversal and MUSIC. available at http://www.ece.neu.edu/faculty/devaney/preprints/paper02n_00.pdf, 1999.

[17] O. Dorn, H. Bertete-Aguirre, J. G. Berryman, and G. C. Papanicolaou. A nonlinear inversion method for 3D electromagnetic imaging using adjoint fields. *Inverse Problems*, 15(6):1523–1558, 1999.

[18] O. Dorn and D. Lesselier. Level set methods for inverse scattering. *Inverse Problems*, 22(4):R67–R131, 2006.

[19] T. M. Habashy, R. W. Groom, and B. R. Spies. Beyond the Born and Rytov approximations: a nonlinear approach to electromagnetic scattering. *J. Geophys. Res.*, 98(B2):1759–1775, 1993.

[20] T. Hohage. Fast numerical solution of the electromagnetic medium scattering problem and applications to the inverse problem. *J. Comput. Phys.*, 214(1):224–238, 2006.

[21] T. Hohage and S. Langer. Acceleration techniques for regularized Newton methods applied to electromagnetic inverse medium scattering problems. *Inverse Problems*, 26(7):074011, 15 pp., 2010.

[22] K. Ito, B. Jin, and J. Zou. A direct sampling method to an inverse medium scattering problem. *Inverse Problems*, 28(2):025003, 11 pp., 2012.

[23] K. Ito, B. Jin, and J. Zou. A two-stage method for inverse medium scattering. *J. Comput. Phys.*, 237:211–223, 2013.

[24] A. Kirsch. The MUSIC algorithm and the factorization method in inverse scattering theory for inhomogeneous media. *Inverse Problems*, 18(4):1025–1040, 2002.

[25] A. Kirsch and N. Grinberg. *The Factorization Method for Inverse Problems*. Oxford University Press, Oxford, 2008.

[26] A. Lakhal. A decoupling-based imaging method for inverse medium scattering for Maxwell's equations. *Inverse Problems*, 26(1):015007, 17 pp., 2010.

[27] A. Lakhal and A. K. Louis. Locating radiating sources for Maxwell's equations using the approximate inverse. *Inverse Problems*, 24(4):045020, 18 pp., 2008.

[28] J. Li and J. Zou. A direct sampling method for inverse scattering using far-field data. *Inverse Problems and Imaging*, 2012, in press. Available at arXiv:1206.0727.

[29] R. Potthast. A survey on sampling and probe methods for inverse problems. *Inverse Problems*, 22(2):R1–R47, 2006.

[30] R. Potthast. A study on orthogonality sampling. *Inverse Problems*, 26(7):074015, 17 pp., 2010.

[31] Y. Saad. *Iterative Methods for Sparse Linear Systems*. SIAM, Philadelphia, PA, second edition, 2003.

[32] H. Tortel, C. Micolau, and M. Saillard. Decomposition of the time-reversal operator for electromagnetic scattering. *J. Electr. Waves Appl.*, 13:687–719, 1999.

[33] M. Vögeler. Reconstruction of the three-dimensional refractive index in electromagnetic scattering by using a propagation-backpropagation method. *Inverse Problems*, 19(3):739–753, 2003.

[34] W. C. Wang, Y. M.and Chew. An iterative solution of the two-dimensional electromagnetic inverse scattering problem. *Int. J. Imag. Sys. Tech.*, 1(1):100–108, 1989.

[35] C. Weber and P. Werner. Regularity theorems for Maxwell's equations. *Math. Methods Appl. Sci.*, 3(4):523–536, 1981.